ORIGINAL PAPER

Outstanding ferroelectric properties in the narrow bandgap cobalt-substituted BiFeO$_3$ spin-coated films

Jing Zhang[1] · Jian-Qing Dai [ORCID][1] · Guang-Cheng Zhang[1] · Xin-Jian Zhu[1]

Abstract

Thin films of BiFe$_{1-x}$Co$_x$O$_3$ (BFCO, $x = 0$–0.05) were prepared using the sol–gel method and deposited on a fluorine-doped tin oxide (FTO)/glass substrate. The crystal structure, surface morphology, dielectric properties, polarization, and optical characteristics of the BFCO thin films were investigated. X-ray diffraction (XRD) and Raman spectroscopy analyses show that Co doping induces lattice distortion. Scanning electron microscopy (SEM) images demonstrate that BFCO films with $x = 0.03$ possess uniform fine grains, which are crucial for their ferroelectric properties. From XPS pattern, it can be observed that Co doping can inhibit the conversion of Fe^{3+} into Fe^{2+}, and BiFe$_{0.97}$Co$_{0.03}$O$_3$ films exhibit greatly reduced oxygen vacancy concentration. Therefore, BiFe$_{0.97}$Co$_{0.03}$O$_3$ film was found to have the lowest leakage current density ($J = 7.18 \times 10^{-7}$ A/cm^2). The film demonstrates outstanding residual polarization at room temperature, with a value of $P_r = 152.1$ μC/cm^2, more than twice the magnitude of that in pure BFO ($P_r = 72.33$ μC/cm^2). Moreover, the dielectric properties of BFCO films show a significant improvement when compared to those of pure BFO samples. This enhancement is attributed to the Co doping-induced structural transition, along with a reduction in grain size and a decrease in the concentration of oxygen vacancies. Additionally, the BiFe$_{0.97}$Co$_{0.03}$O$_3$ film exhibits a narrower band gap ($E_g = 1.69$ eV) in comparison to the BFO film ($E_g = 1.87$ eV). Consequently, an expansion in the range of photovoltaic applications for BFO films can be achieved.

✉ Jian-Qing Dai
  djqkust@sina.com

[1] Faculty of Materials Science and Engineering, Kunming University of Science and Technology, Kunming 650093, PR China

Graphical Abstract

Fig 1. **a**–**f** Ferroelectric hysteresis loops of the BFCO thin films. Fig 2. **a** UV–Vis absorption spectra of the BFCO thin films. **b** Tauc curves of the BFCO thin films.
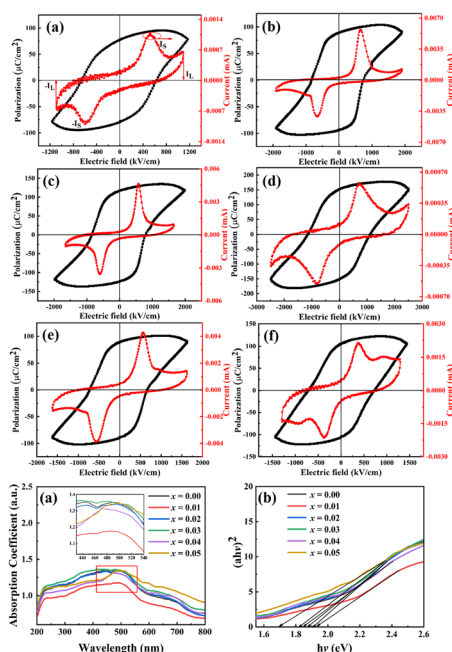
Highlights

- $BiFe_{1-x}Co_xO_3$ (BFCO, $x = 0$–0.05) thin films on a fluorine-doped tin oxide (FTO)/glass substrate were prepared through the sol–gel method.
- $BiFe_{0.97}Co_{0.03}O_3$ was found to have the lowest leakage current density ($J = 7.18 \times 10^{-7}$ A/cm²), with excellent remnant polarization at room temperature which is more than twice as large as that of pure BFO.
- The bandgap ($E_g = 1.69$ eV) was reduced by doping BFO with Co.

1 Introduction

Multiferroic materials simultaneously possess two or more ferromagnetic orders, such as ferroelectricity, ferromagnetism, ferroelasticity, and ferrotoroidicity, which result in a diverse range of physical phenomena [1, 2]. These properties not only open up new avenues of research in condensed matter physics but also hold significant promise for a range of applications, including new information storage media, spintronics, ultrafast optoelectronic devices, piezoelectric nanogenerators and ferroelectric random access memories [3–5]. Bismuth ferrite (BiFeO₃), known as BFO, is widely recognized as the most significant single-phase multiferroic material at room temperature due to its simultaneous exhibit of ferroelectricity and ferromagnetism [6, 7].

BFO possesses high Curie temperature ($Tc \sim 830\,°C$) and high Néel temperature ($T_N \sim 370\,°C$). In addition, the theoretical ferroelectric polarization value is as high as $100\,\mu C/cm^2$, which makes it one of the most promising multiferroics [8–12]. With the emphasis on new environmentally friendly functional materials, BFO lead-free films have become a research focus. However, due to the high-temperature volatilization of Bi^{3+} ions and the fluctuation of valence state of Fe ions (from Fe^{3+} to Fe^{2+}) during the films' preparation, BFO films usually show high concentrations of oxygen vacancy defects, resulting in large leakage current and poor ferroelectric properties [13–17]. To improve the ferroelectric properties, researchers have employed various methods such as ion substitution, structural domain control, chemical modification processes, and composites [18–22]. Among them, ion doping substitution is a simpler, lower cost, and more efficient method. Transition metal ions such as Cu, Zn, Ti, Mn, Co, etc. can be used to replace Fe^{3+} or Bi^{3+}, causing a certain degree of lattice distortion and

altering the carrier concentration, leading to high-performance [23–26]. As the ionic radii of Fe^{3+} and Co^{2+} are similar, a small amount of Co^{2+} can replace Fe^{3+} ions in $BiFeO_3$. Substitution of lower-priced elements requires charge compensation, which can be met by the creation of anionic (oxygen) vacancies or an increase in cationic valence (Fe^{2+}-Fe^{3+}), thus suppressing valence fluctuations from Fe^{3+} to Fe^{2+}. Thus, low-priced dopants can lead to a decrease in the band gap due to an increase in the defect-induced energy level or state density within the band gap. Low (2+) ion substitution also provides the possibility for the production of defective dipoles, which can therefore lead to drastic changes in various physical properties [27]. Co^{2+} serves as a dopant substitution element and its substitution role may be of great interest. Xue et al. reported that by co-doping with Gd and Co, the ferroelectric properties of the BFO thin film were further enhanced ($P_r = 101\ \mu C/cm^2$, $E_c = 345\ kV/cm$) [28]. Ghanshyam et al. successfully prepared a $Bi_{0.99}Sm_{0.01}Fe_{0.99}Co_{0.01}O_3$ thin film through the sol–gel method, achieving a low leakage current density of $10^{-7} A/cm$ [29]. Sinha et al. synthesized Co-doped BFO thin films via the sol–gel method, and the results showed that as the Co^{2+} doping level increases in the BFO lattice, the size of the pristine $BiFeO_3$ NPs gradually decreases, and Co doping enhances the magnetic and dielectric properties to a greater extent [30]. Saha et al. induced ferromagnetic properties in Co modified BF-PT and provided guidance for understanding the electromechanical response in BFO-based alloys [31]. Wani et al. used sol–gel methods to prepare pure BFO and Co-doped BFO nanostructured materials, systematically studying the influence of Co substitution on the structure, morphology, dielectric, and optical properties of BFO. The results showed that $BiFe_{1-x}Co_xO_3$ ($x = 0.00$, 0.03, 0.05, 0.10) all displayed a perovskite structure. With the increase of doping level, the average grain size enlarges, and the induced strain initially decreases and then strengthens [32]. As a result, Co doping significantly enhanced the physical properties of BFO films. The single-ion substitution method has also become an efficient method for obtaining excellent multiferroic properties in BFO films. These results are of extraordinary significance for the application of BFO.

In order to demonstrate the impact of Co doping on the ferroelectric properties of BFO thin films, we prepared thin films of $BiFe_{1-x}Co_xO_3$ (BFMO) with Co doping concentrations ($x = 0$–0.05) on fluorine-doped tin oxide (FTO)/glass substrates using the sol–gel method. By controlling the doping level, the ferroelectric and dielectric properties can be adjusted to achieve specific functional applications. As doping increases, the oxygen vacancy content decreases leading to improved ferroelectric properties, dielectric properties, and photovoltaic performance.

2 Experiment

Using the sol–gel technique, spin coated films of $BiFe_{1-x}Co_xO_3$ (BFCO) with various Co doping levels ($x = 0$, 0.01, 0.02, 0.03, 0.04, and 0.05) were prepared on FTO/glass substrates. The precursor raw materials were analytically pure $Fe(NO_3)_3 \cdot 9H_2O$, $Bi(NO_3)_3 \cdot 5H_2O$ and $Co(NO_3)_2 \cdot 6H_2O$. A 4% excess of bismuth is used to compensate for the effects caused by bismuth volatilization during high-temperature annealing. The precursor solution was prepared by weighing according to the desired stoichiometric ratio and dissolving in organic solvents (ethylene glycol monomethyl ether and glacial acetic acid) with a volume ratio of 1:3 (overall Bi concentration of 0.25 M). The mixture was continuously stirred at a constant speed for 1 h at room temperature to ensure complete dissolution. Citric acid monohydrate ($C_6H_8O_7$, as a chelating agent; 0.25 M), ethylene glycol ($C_2H_6O_2$, serving as a dispersant, 12 ml), and ethanolamine (C_2H_7NO, stabilizer and a viscosity modifier, 0.5 ml) were then sequentially added to the aforementioned mixture. The resulting solution was stirred continuously for 2.5 h at room temperature to obtain a homogeneous precursor with a solution concentration of 0.25 M with respect to Bi. The precursor solution was aged for 48 h to promote hydrolysis and polymerization within the solution. The FTO/glass substrates were sequentially cleaned with acetone, alcohol, and deionized water through ultrasonic cleaning. The precursor solutions with different Co contents were dropped onto the substrate and spin-coated at 2000 rpm for 15 s to obtain the initial wet film. To remove water and organic solvents, the deposited thin film were placed in a constant temperature oven set at 85 °C for a duration of 10 min. Subsequently, it was transferred to a muffle furnace at 550 °C for 10 min to eliminate any remaining organic solvents and initiate the crystallization process of the film. By performing 14 consecutive annealing cycles, the thermal treatment process of the wet film was completed, ultimately resulting in the desired thickness of the BFCO thin film. Subsequently, the coated film was annealed at 550 °C for 30 min to facilitate the full growth of BFO grains. To fulfill the electric properties measurement requirements, Pt dot electrodes with an area of 0.126 mm^2 were deposited through sputtering with the utilization of a shadow mask.

The crystallographic structures of the BFCO thin films were evaluated using X-ray diffraction (XRD) with an Ultima IV diffractometer in grazing incidence mode (angle of incidence = 0.5°). Raman spectroscopy, performed on the prepared film samples using LabRAM HR and a laser wavelength of 633 nm, was employed to analyze their molecular structure. The grain microstructure and cross-sections of the films were observed using scanning electron

microscopy (SEM) with a Zeiss Sigma300 instrument. Furthermore, the sample's elemental composition was analyzed through energy-dispersive X-ray spectroscopy (EDS). XPS (ESCALAB 259xi) was used to further examine the chemical elements and surface compositions of the samples. The polarization-electric field hysteresis loops and the leakage currents were measured using a ferroelectric analyzer (Aix ACCT, TF Analyzer 2000). The optical bandgap was determined using a Hitachi U4100 spectrophotometer, which measured the absorption spectra in the ultraviolet-visible (UV–Vis) range. The dielectric frequency spectra were obtained by analyzing the impedance using a precision analyzer (Agilent 4294A).

3 Results and discussion

3.1 Phase structure and micromorphology

The XRD patterns of the BFCO films are illustrated in Fig. 1. Peaks were located at about 26.6°, 33.8°, and 37.9°, which correspond to SnO_2 (JCPDS no.41-1445). The other diffraction peaks match the standard values reported in JCPDS No. 72-2112, and the $R3c$ rhombic perovskite BFCO structure is detected. No peaks associated with impurities were detected beyond the 20–60° range in relation to the perovskite structure. This is due to the thermal annealing process and appropriate content of bismuth and iron ions. Figure 1a indicates that all six samples possessed an identical single-phase structures, and the results show that the doping did not affect the lattice symmetry [33]. Figure 1b depicts a magnified partial view of the XRD pattern, specifically highlighting the range of ~31–33°. The diffraction peaks at (012) and (110) orientations in pure

BFO demonstrate a bimodal characteristic. Upon the Co^{2+} substitution, the (110) peak exhibits a reduced angular displacement and diminished intensity, suggesting the partial replacement of Fe ions by the doped ions within the BF lattice structure. This results in a single peak formed by the merging of the (012) and (110) peaks. Additionally, the similar merging of XRD peaks and angular shifts could suggest that the doping of Co^{2+} might induce distortion in the lattice structure of the BFCO thin films. This is attributed to the mismatch in ionic radii, as Co^{2+} ions possess a larger radius (0.740 Å) in comparison to Fe^{3+} ions (0.645 Å). This results in slight changes in the interplanar spacing and grain size within the BFCO lattice as the Co doping content increases. The diffraction peak positions remain almost constant when the content of Co exceeds 0.04, which may be due to the fact that Co is a variable valence ion. In this regard, it is noteworthy that the enhancement of ferroelectric properties in thin films may be strongly correlated with lattice deformation and ion valence states [34, 35]. Table 1 lists the changes in lattice parameters (a and c) and volume. The variations in a and c are related to the doping level of Co, indicating a significant alteration in the film structure. The increase in the volume of the BFO crystal unit cell is attributed to the larger ion radius of Co^{2+} (0.740 Å) compared to that of Fe^{3+} (0.645 Å).

The sample was examined through Raman scattering analysis in Fig. 2, which possesses a strong sensitivity to the crystal structure and provides complementary information to that of XRD characterization. To accurately determine the peak position for each Raman vibration mode, the Raman spectra of the BFCO films from 50 to 800 cm^{-1} were fitted using a Lorentz model. The rhomboid perovskite structure consists of 4 A_1 vibration modes and 9 E vibration modes [36, 37]. There are nine distinct Raman spectroscopic patterns observed in the films. The vibrations of Bi-O primarily occurs in the low-wavenumber region corresponding to the A modes, while the E modes in the high-wavenumber region are related to the vibrations of Fe-O [38]. Ion doping has a significant effect on the vibrational intensity and position of Bi-O and Fe-O modes, with the intensity and position of the A_1-1 and A_1-2 peaks of the Co-
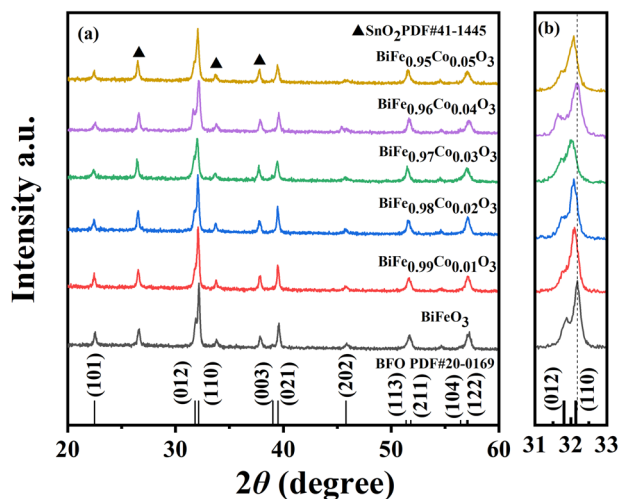

Fig. 1 a XRD patterns of BFCO thin films. b Partially enlarged pattern in the 2θ range of 31–33°

Table 1 Cell parameters of the BFCO thin films

Samples	Cell parameters (a/c)	Volume (Å³)	Symmetry
$BiFeO_3$	5.577 13.861	373.4	R_{3c}(161)
$BiFe_{0.99}Co_{0.01}O_3$	5.577 13.863	373.3	R_{3c}(161)
$BiFe_{0.98}Co_{0.02}O_3$	5.578 13.863	373.5	R_{3c}(161)
$BiFe_{0.97}Co_{0.03}O_{33}$	5.587 13.867	374.9	R_{3c}(161)
$BiFe_{0.96}Co_{0.04}O_3$	5.579 13.862	373.5	R_{3c}(161)
$BiFe_{0.95}Co_{0.05}O_3$	5.586 13.741	371.3	R_{3c}(161)

doped samples were different compared to the pure BFO. With the increase of Co doping concentration, the A_1-1 and A_1-2 vibration modes tend to merge into a single mode. This is due to the change in the length of the Bi-O bond and the angle of the Bi-O-Bi bond, caused by the substitution of Co^{2+} ions for Fe^{3+} ions. The change in the E mode confirms that Co partially replaces Fe in the BFO lattice. In addition, the intensity of the A_1-4 and E-9 vibration peaks in the BFCO thin film gradually increases, and the intrinsic vibration mode of Fe-O bond partially changes to that of the Co-O bond. Therefore, the structural distortion of the FeO_6 octahedron increases. On the other hand, due to the Jahn-Teller effect, the mismatch of radii between Co and Fe ions leads to severe distortion of the iron oxide octahedron [39, 40]. The results indicate that Co doping leads to changes in the bond length and bond angle of the Fe-O bond and indirect changes in the Bi-O bond, which cause a change in the lattice of the film, consistent with the XRD results. These data are summarized in Table 2.
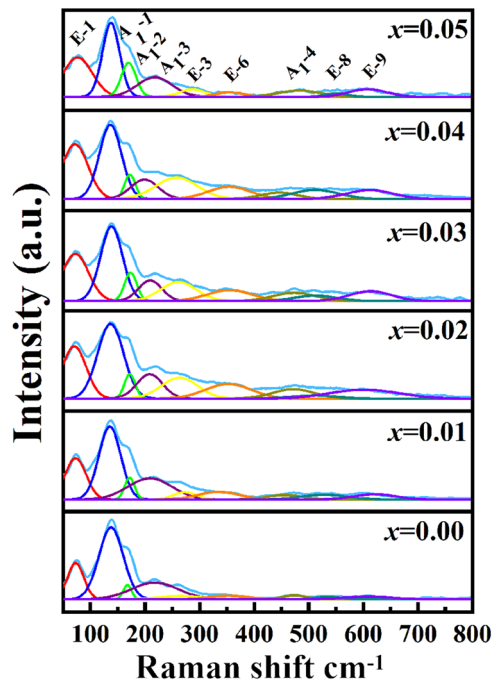

Fig. 2 Raman spectra of the BFCO thin films

Synthesis conditions and doping are known to alter surface microstructure and grain growth, thereby affecting material properties. The surface morphology of BFCO and partial section morphology of BFCO films ($x = 0$, 0.03) are displayed in Fig. 3. As shown in the figure, the six films have good crystallization, and appear flat and smooth without cracks; nevertheless, some pinhole defects were scattered on the sample surface due to volatilization of organic substances and Bi ions during annealing. Some grain clusters appeared in the BFCO film with Co doping, which may be due to the obvious effect of the introduction of Co ion on grain growth, especially the sample of $x = 0.03$ (Fig. 3d) [41, 42]. The average grain size of BFCO-0 (Fig. 4a) and BFCO-3 thin films (Fig. 4b) is 90 nm and 78 nm, respectively, according to the histogram of particle size distribution. The results demonstrate that the optimal level of Co ion doping exerts a favorable influence on the enhancement of grain growth. For BFO films, grain size is closely related to lattice distortion and electrical properties, which also confirms the XRD correlation analysis. In the cross-sectional morphology of BFCO-0 and BFCO-3 films shown in Fig. 3a, d, respectively, it can be observed that there is a clear layered structure without mutual diffusion between the film and the FTO substrate. The thicknesses of the BFCO-0 and BFCO-3 films were measured to be 1.4 μm and 1.3 μm, respectively. Due to the use of specific FTO/glass substrates, all films have a specific thickness of 1.1 μm of FTO layer underneath. The improved compactness of the film structure also has an impact on the reduction of its leakage current density [43, 44]. The composition of $BiFe_{0.97}Co_{0.03}O_3$ was analyzed by EDS, and its elemental energy spectrum and mapping map are shown in the Fig. 3g, h. In addition to the adventitious carbon coating used for SEM characterization, only the elements Bi, Fe, Co, and O were detected in the sample. Moreover, these elements exhibited uniform distribution throughout the sample. The atomic content of each element in the prepared $BiFe_{0.97}Co_{0.03}O_3$ thin film sample is basically consistent with the stoichiometric ratio of BFCO, which directly indicates that Co has been successfully incorporated into the BFO lattice. The above results combined
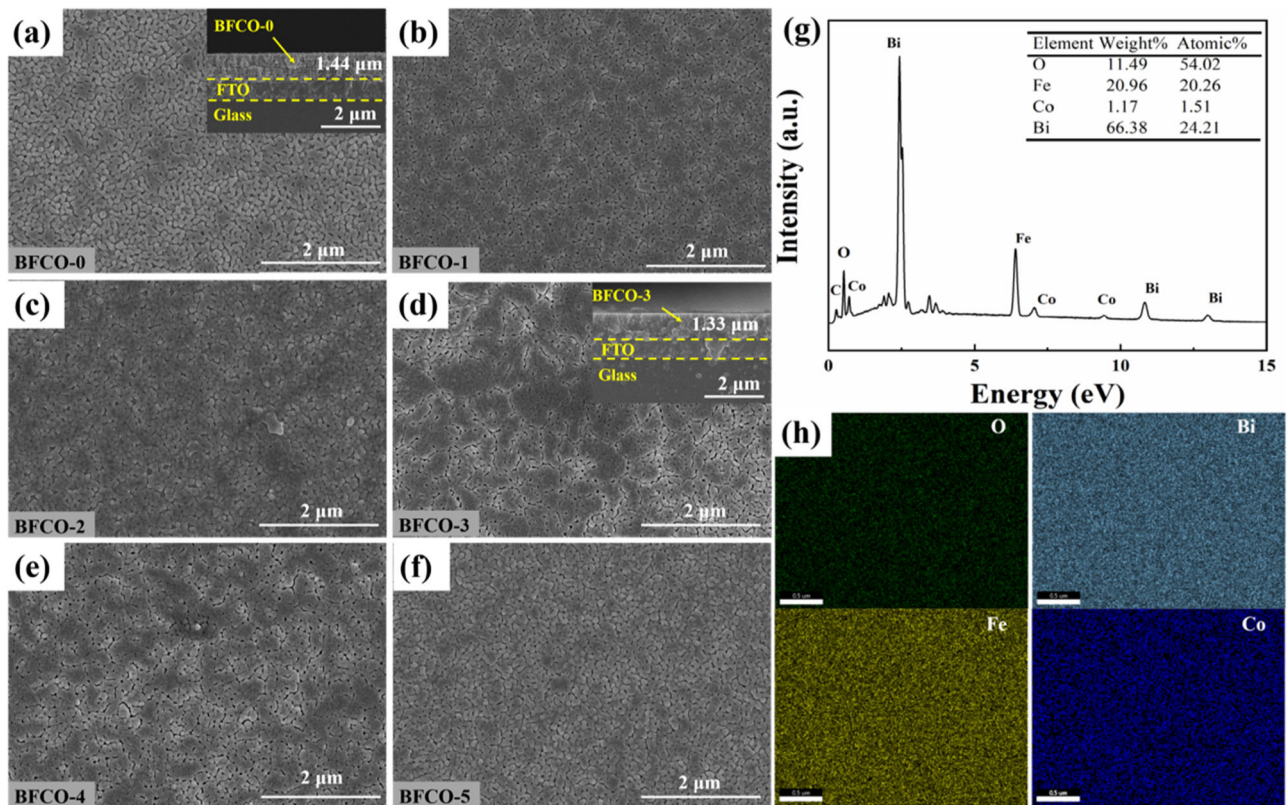
Table 2 Laman parameters of the BFCO thin films

$BiFe_{1−x}Co_xO_3$	E-1	A_1-1	A_1-2	A_1-3	E-3	E-6	A_1-4	E-8	E-9
$x = 0.00$	70.6	137.0	172.3	208.7	263.3	352.6	472.0	510.0	602.0
$x = 0.01$	72.1	136.7	172.6	199.2	257.8	354.3	445.9	512.0	611.5
$x = 0.02$	73.1	135.7	171.9	209.3	272.8	334.8	456.4	528.4	621.2
$x = 0.03$	77.1	137.8	170.0	218.0	286.9	355.0	483.1	551.3	608.0
$x = 0.04$	72.6	137.8	172.7	205.8	266.0	347.7	474.0	511.0	614.0
$x = 0.05$	71.9	136.9	172.3	206.1	265.8	347.1	473.0	511.8	613.8

Fig. 3 a–f Surface morphology image of $BiFe_{1-x}Co_xO_3$ ($x = 0$–0.05) films. The insets in (**a**) and (**d**) show cross-sectional micrographs of pure BFO and $BiFe_{0.97}Co_{0.03}O_3$ films. **g** EDS spectral pattern of $BiFe_{0.97}Co_{0.03}O_3$ film. **h** Elemental mapping of Bi, Fe, Co, and O for $BiFe_{0.97}Co_{0.03}O_3$ film
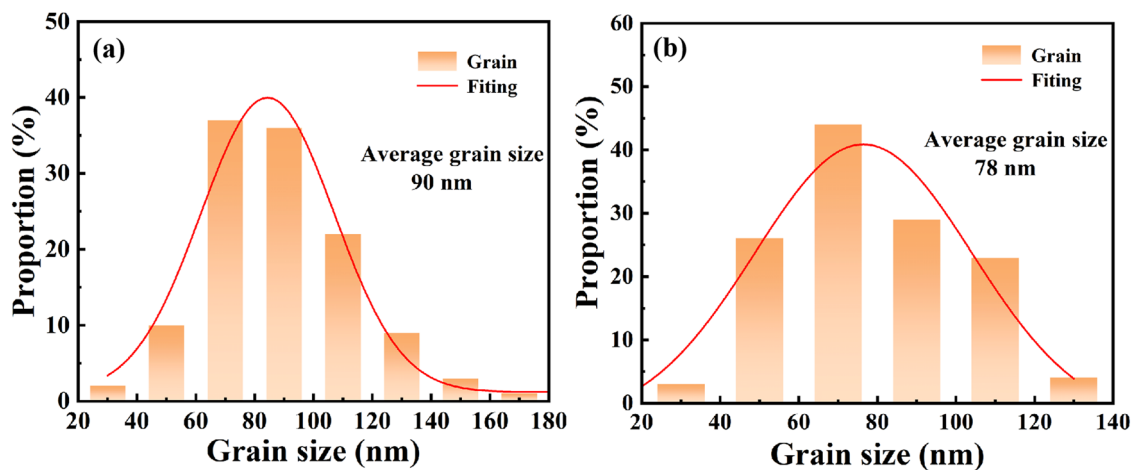

Fig. 4 Histogram of particle size distribution of (**a**) BFCO-0 and (**b**) BFCO-3 thin films

with XRD analysis directly confirmed the presence of Co ions and the successful Co doping of BFO.

The ferroelectric performance of the films is influenced not only by its growth orientation but also by any defects present, such as oxygen vacancies [45]. The surface elemental chemical states of the thin films were determined by conducting XPS measurements, as depicted in Fig. 5. The characteristic peaks are clearly discernible, and detailed

information regarding the element content is provided in Table 3. Since the experimental samples themselves do not contain the element C, the binding energy was first calibrated by a charge shift based on C1s = 284.8 eV. In Fig. 5a, the presence of a double peak in the low binding energy region of Fe indicates the coexistence of both Fe^{2+} and Fe^{3+} in the thin film. Moreover, the ratio of Fe^{3+} to Fe^{2+} directly impacts the electronic and valence states of the film. In the
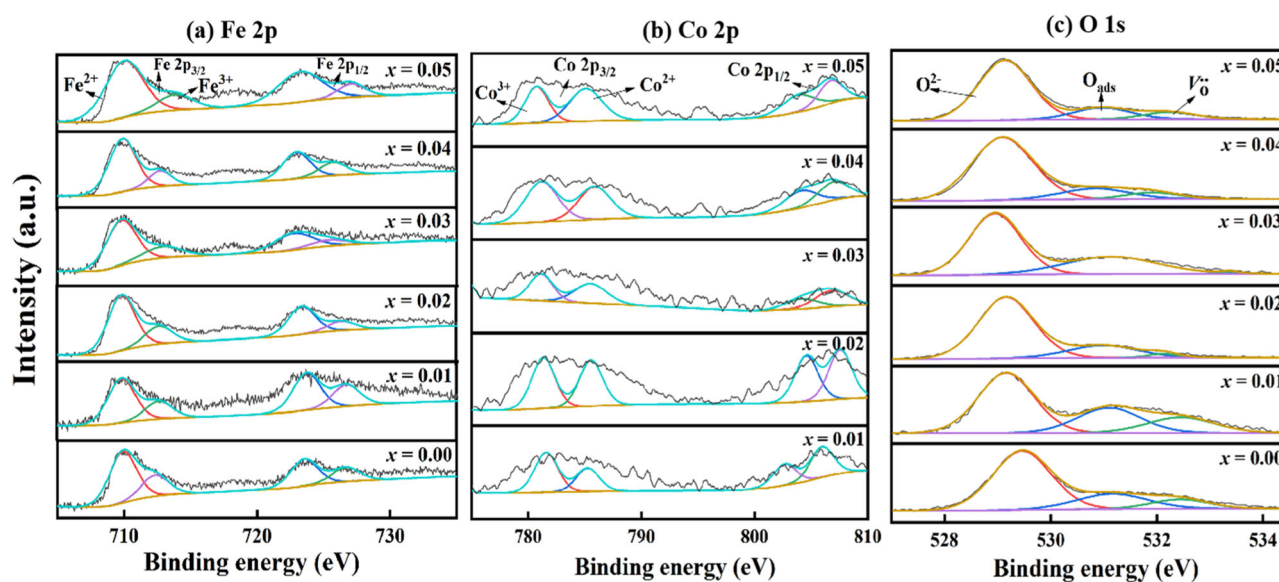
Fig. 5 **a** Fe 2p spectrum of BFCO thin films. **b** Co2p spectrum of BFCO thin films. **c** O1s spectrum of BFCO thin films
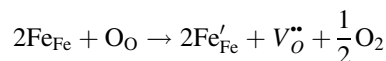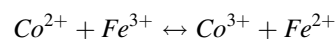
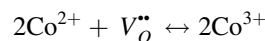Table 3 XPS peak area ratio of the BFCO thin films

$BiFe_{1-x}Co_xO_3$	$Fe^{2+}: Fe^{3+}$	$O^{2-}:O_{abs}:V_O^{\bullet\bullet}$	$Co^{2+}: Co^{3+}$
$x = 0.00$	71.53:28.47	66.13:19.67:14.20	——
$x = 0.01$	71.35:28.65	63.07:18.22:18.71	52.36:47.64
$x = 0.02$	72.98:27.02	76.50:14.91:8.59	47.55:52.45
$x = 0.03$	64.15:35.85	75.15:19.21:7.64	37.10:62.90
$x = 0.04$	73.35:26.65	77.21:13.57:9.22	54.73:45.27
$x = 0.05$	79.40:20.60	71.84:16.67:11.49	56.25:43.75

thin films, due to the presence of Fe^{2+}, a certain number of oxygen vacancies will be generated to maintain charge balance. Thus, the concentration of Fe^{2+} ions is correlated with the number of oxygen vacancies [46, 47]. Through the analysis results, the surface Fe^{2+} content of BFCO films ($x = 0$, 0.01, 0.02, 0.03, 0.04, 0.05) was found to be 71.5%, 71.4%, 73.0%, 64.2%, 73.4%, and 79.4%, respectively. In the $BiFe_{0.97}Co_{0.03}O_3$ film, the Fe^{2+} content is the lowest, which also indicates that Co doping is beneficial in inhibiting the conversion of Fe^{3+} to Fe^{2+}.

In Fig. 5b, corresponding to the Co2p orbital satellite peaks (namely $Co2p_{3/2}$ and $Co2p_{1/2}$), the presence of both divalent Co and trivalent Co is observed. It is found that the multivalent Co undergoes a valence state transition after heat treatment. Quantitative analysis reveals that the Co^{2+}/Co^{3+} ratio of the $BiFe_{0.97}Co_{0.03}O_3$ film is 37.1/62.9. The presence of Co^{2+} leads to the formation of oxygen vacancies. The oxygen vacancies combine with defect dipoles to form defect complexes ($Co'_{Fe} - V_O^{\bullet\bullet}$) and help balance the charge concentration. However, with the introduction of Co^{3+}, there is a gradual increase in the conversion of Co^{2+}

to Co^{3+}, effectively inhibiting the generation of oxygen vacancies. The details of this conversion are shown in the following equations.

$$2Co^{2+} + V_O^{\bullet\bullet} \leftrightarrow 2Co^{3+}$$

$$Co^{2+} + Fe^{3+} \leftrightarrow Co^{3+} + Fe^{2+}$$

$$2Fe_{Fe} + O_O \rightarrow 2Fe'_{Fe} + V_O^{\bullet\bullet} + \frac{1}{2}O_2$$

The O1s spectrum is shown in Fig. 5c and consists of three parts. The peak at ~531 eV corresponds to lattice oxygen (O^{2-}), while the peak in the middle at ~532 eV represents surface-adsorbed oxygen originating from the surface metal atoms and chemisorbed species [48]. The last peak at ~533 eV corresponds to adsorbed oxygen. All BFCO films contain oxygen vacancies, which directly affect their ferroelectric properties [49]. As the Co doping level increases, the concentration of oxygen vacancies in BFCO thin films gradually decreases. In the $BiFe_{0.97}Co_{0.03}O_3$ thin film, the concentration of oxygen vacancies is reduced to 7.6%. This is attributed to the charge balance effect between Fe^{2+} and Co^{3+}. When the Co content increases to 0.05, the oxygen vacancy content in the thin film increases significantly to 11.5%, indicating that the Fe^{2+} and oxygen vacancy content is the lowest in the $BiFe_{0.97}Co_{0.03}O_3$ thin film. Through XRD combined with XPS analysis, it is demonstrated that Co ions are efficiently doped into the BFO lattice, and there is a valence state transition of Co^{2+}, resulting in the presence of a large number of Co^{3+} ions in the BFCO thin film. From this, it can be concluded that a certain amount of Co doping can effectively suppress the

formation of oxygen vacancies, and the impact on the thin film leakage current density will be discussed in detail in the following sections [50].

3.2 Physical properties

Figure 6a–f shows the hysteresis loops and polarization current curves of $BiFe_{1-x}Co_xO$ ($x = 0.00–0.05$) thin films, while details of the P_r values are presented in Table 4. The red curve in the figure is the I-E curve from which the switching current (I_S) and the polarization leakage current (I_L) of all film samples are obtained. The I_S value reflects the difficulty of ferroelectric domain reversal. The larger the I_S value, the easier the ferroelectric domain reversal and the stronger the spontaneous polarization of the film. The I_L value represents the bias of the polarization leakage current and reflects the degree of polarization leakage. The higher the I_L value, the greater the polarization contribution from non-
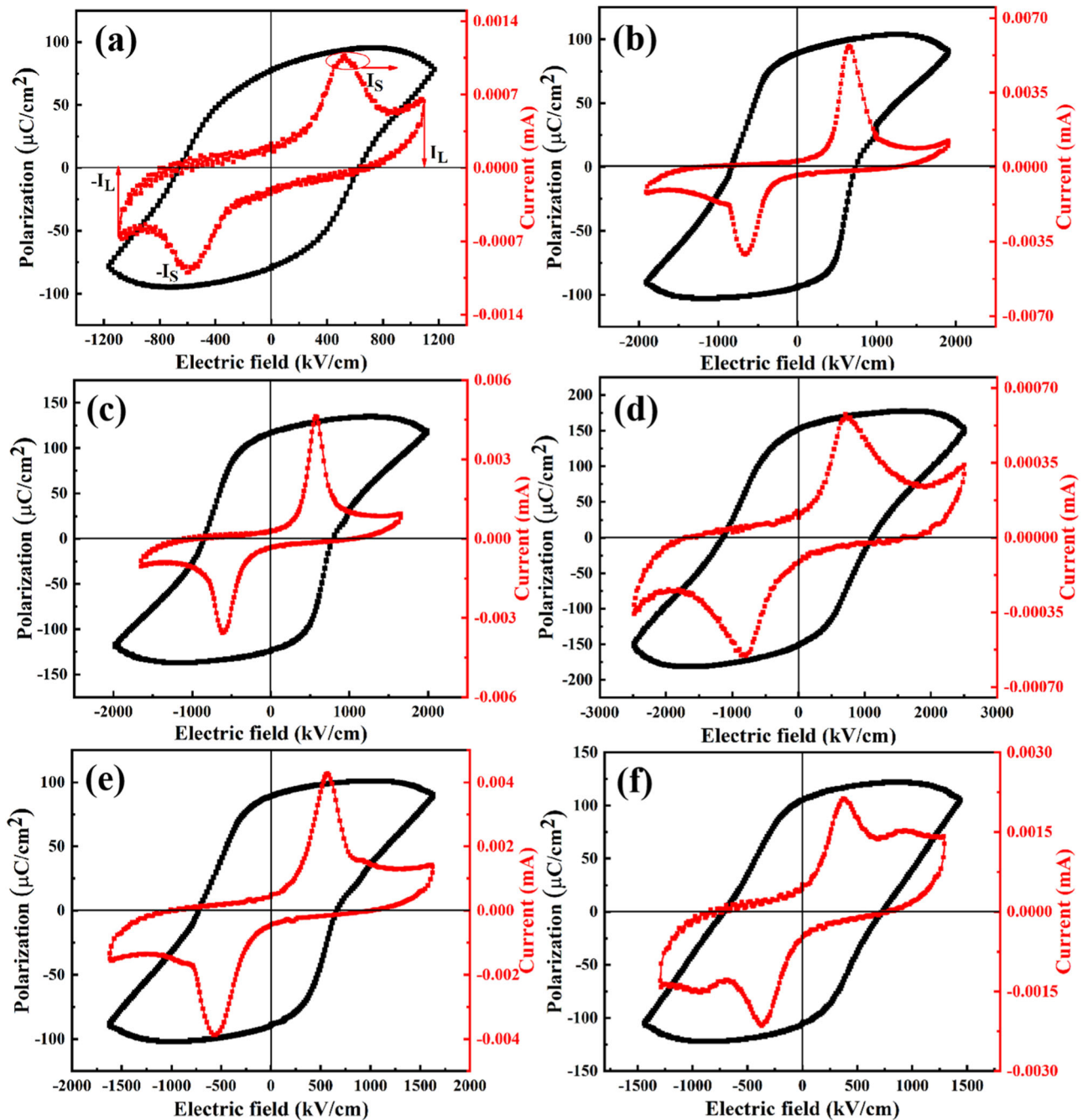

Fig. 6 a–f Ferroelectric hysteresis loops and polarization current curves of the BFCO thin films

intrinsic leakage. The minimum I_S value of BFCO-0 is 1.07×10^{-3} mA and the minimum I_L value of BFCO-3 is 3.4×10^{-4} mA, which corresponds to the lowest leakage current density of BFCO-3. From the current curve, it can be seen that the ferroelectric domain inversion of BFO films is significantly enhanced by appropriate Co doping. Compared to BFCO thin films, BFO exhibits an unsaturated circular hysteresis loop with a low residual polarization value of 72.33 μC/cm^2. It can be seen that the BFCO film exhibits a rectangular *P-E* loop and a higher *P*r value than the BFO film. The remnant polarization value of the BFCO film increases with the increase of dopant concentration. The residual polarization value of BFCO films also increases with the increase in dopant concentration, indicating that the doping of Co can effectively enhance the ferroelectric performance. Among them, the BiFe$_{0.97}$Co$_{0.03}$O$_3$ thin film sample has the highest residual polarization value of $P_r \approx 152.1$ μC/cm^2, with a coercive field of $E_c \approx 554.7$ kV/cm. This could be attributed to the increased susceptibility of ferroelectric domains to switching under high electric fields. We speculate that the ultra-high polarization of the BFCO thin film may be attributed to three reasons. Firstly, the substitution of Co^{2+} influences the lattice distortion caused by the mismatch in the ionic radii of Fe and Co, thus increasing the tendency favorably for spontaneous polarization. Secondly, the large residual polarization value may be attributed

to the increase in thin film density due to the reduction in grain size, which in turn reduces the leakage current density. As the leakage current decreases, the residual polarization gradually increases. Thirdly, combined with XPS analysis, it is shown that the doping of Co at the Fe sites in BFO inhibits the generation of oxygen vacancies, thereby improving the ferroelectric performance of the thin film [51, 52]. When the Co content exceeds $x = 0.03$, the residual polarization value of the thin film shows a decreasing trend. This phenomenon is likely due to the increase in leakage current with the increase in grain size and defect density, which in turn leads to a deterioration in its ferroelectric behavior.

In fact, the *P-E* data of the BFCO thin films may be influenced by the leakage current density and nonlinear dielectric characteristics, and hence further analysis is required [53]. The ferroelectric test was conducted to determine the intrinsic polarization of the BFCO thin films, as shown in Fig. 7a. It is well known that $\Delta P = P_{sw} - P_{nsw} = 2P_r$, where P_{sw} represents the switching polarization and P_{nsw} represents the non-switching polarization. At the highest voltage, the pulse residual polarization values (ΔP) of BFCO ($x = 0$–0.05) thin films are: 108.31, 156.69, 195.10, 223.33, 106.54, and 85.25 μC/cm^2, respectively. From the analysis of the graphs, it can be observed that the trend of ΔP values is consistent with the *P-E* data. However, it is evident that the ΔP value is smaller than the $2P_r$ value of the BFCO thin film, indicating that the influence of leakage current on the ferroelectric behavior of the material cannot be ignored.

The insulation properties of BFCO thin films were tested within the range of 0–250 kV/cm, and a curve of the sample leakage current density varying with the applied electric field was plotted. As a result of the aforementioned factors, including oxygen vacancies, the concentration of Fe^{2+} ions and grain boundaries, the current density of thin films made of BFCO is low at low electric fields but increases rapidly at high electric fields, as illustrated in Fig. 7b. The *J* values of BiFe$_{1-x}$Co$_x$O$_3$ ($x = 0.00$–0.05) films are 2.45×10^{-5},

Table 4 Ferroelectric and dielectric parameters of the BFCO thin films

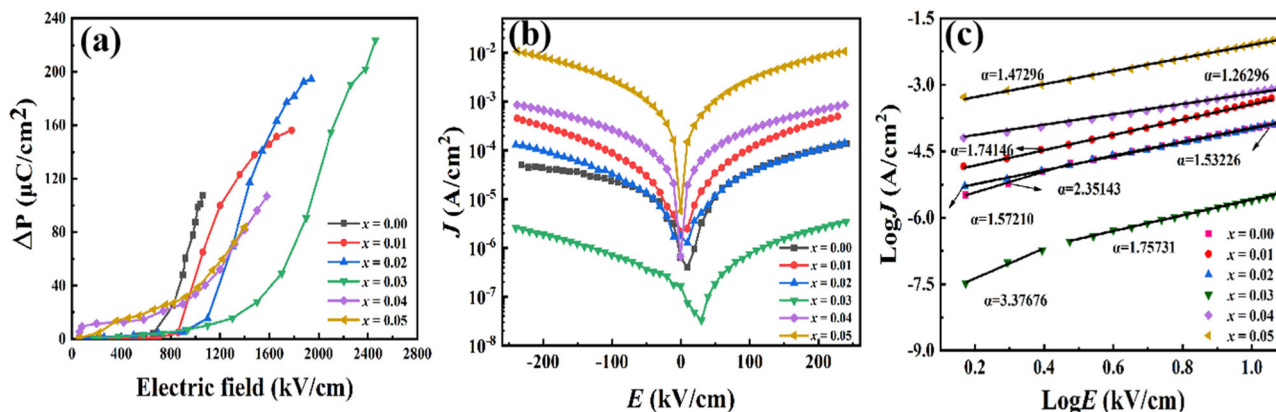| BiFe$_{1-x}$Co$_x$O$_3$	$2P_r$ (μC/cm^2)	ΔP (μC/cm^2)	J (A/cm^2)	ε_r	tanδ
$x = 0.00$	144.66	108.31	2.45×10^{-5}	30.04	0.168
$x = 0.01$	178.34	156.69	8.79×10^{-5}	38.68	0.202
$x = 0.02$	233.40	195.10	3.27×10^{-5}	45.47	0.175
$x = 0.03$	304.20	232.33	7.18×10^{-7}	74.89	0.156
$x = 0.04$	178.44	106.54	2.64×10^{-4}	46.87	0.161
$x = 0.05$	210.20	84.25	2.81×10^{-3}	65.64	0.224

Fig. 7 **a** Pulsed polarization of the BFCO thin films; **b** Leakage current density; and (**c**) log *E* vs log *J* functional diagrams of the BFCO thin films
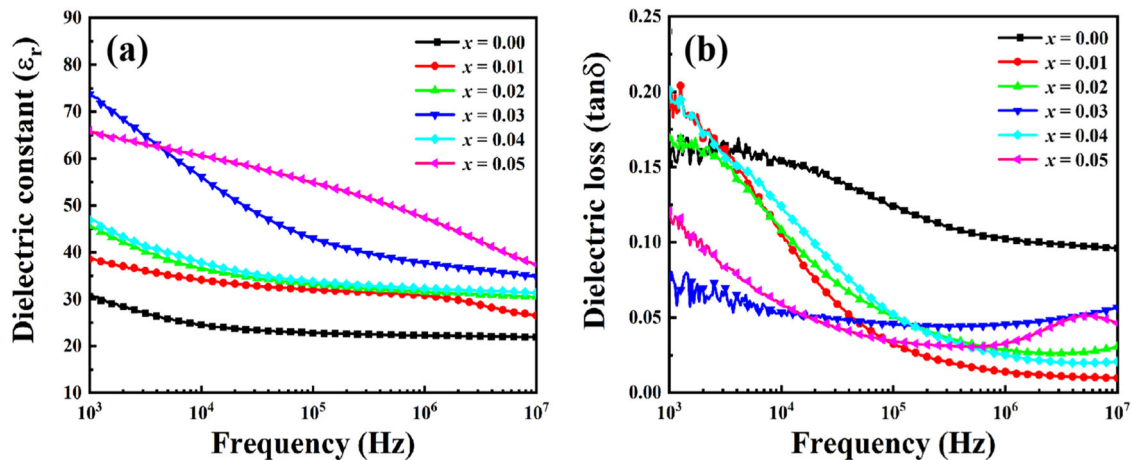
Fig. 8 a ε_r and (**b**) $\tan\delta$ for BFCO thin films at RT

8.79×10^{-5}, 3.27×10^{-5}, 7.18×10^{-7}, 2.64×10^{-4} and 2.81×10^{-3} A/cm^2, respectively The sample with $x = 0.01$ reduced the leakage current density by two orders of magnitude compared with pure BFO samples. Therefore, a certain amount of Co ion doping can effectively reduce the leakage current density of BFO thin films. The origin of the high leakage current in BFO-based materials is the generation of oxygen vacancies. As an electron trapping center, oxygen vacancies can enhance leakage by activating conduction with an externally applied electric field [54]. XPS confirms that Co doping suppresses electron hopping between Fe^{3+} and Fe^{2+} and the generation of oxygen vacancies. At the same time, $Co^{2+}_{Fe^{3+}}$ combines with $V_O^{\bullet\bullet}$ to form defect dipoles that restrict the movement of oxygen vacancies. As another factor that suppresses the increase of leakage current, grain boundaries reduce significantly as Co ions enter the BFO lattice, resulting in large insulation boundaries. Therefore, the grain boundaries also contribute to the reduction of leakage current behavior by serving as a barrier for current conduction. When $x = 0.02–0.05$ mol%, the carrier density in the BFCO thin film increases as the oxygen vacancy content increases, resulting in an increase in J value [55].

In Fig. 7c, to better understand the leakage mechanism of BFCO film, it is necessary to further investigate the conduction mechanism of the sample. For volumetric conduction, leakage includes the effects of both free carriers generated by heat and injected carriers. The leakage current curve was fitted using the volumetric confinement conduction mechanism, and the relationship between $\log(J)$ and $\log(E)$ was analyzed [56]. The conduction mechanism was determined by the slope of the linear correlation, where $\alpha = 1$ for Ohmic conduction and $\alpha \geq 2$ for space charge-limited conduction (SCLC). In the BFCO films with $x = 0.02$, 0.03, 0.04, and 0.05, the leakage current is mainly caused by the Ohmic conduction mechanism, and the curve fitting slopes

are close to 1 (1.57, 1.74, 1.26, and 1.47, respectively). This indicates that intrinsic mobile electrons or holes in BFCO film contribute to conduction. For the thin film samples with $x = 0.00$ and 0.01, the Ohmic conduction mechanism is still the main mechanism, but SCLC is also observed, which may be due to the unequal density of injected carriers and equilibrium carriers that result in a space charge effect [57].

In order to study the dielectric properties of thin films with different Co doping levels, the dielectric constant and dielectric loss values of BFCO thin films were obtained as the frequency varied as shown in Fig. 8. Under the action of an alternating electric field, the space charge undergoes changes, with a relatively large ε_r value, which remains largely unchanged at higher frequencies [58]. As the frequency increases, the oxygen vacancy-related dipoles fail to respond promptly to the changes, resulting in a decreasing trend in the ε_r value. At 1 kHz, the ε_r value of BFO is 30.04, while the ε_r value of $BiFe_{0.97}Co_{0.03}O_3$ is 74.89. The variation in ε_r value is attributed to the reduction in the number of defects such as oxygen vacancies. Figure 8b demonstrates that at lower testing frequencies, the dielectric loss values ($\tan\delta$) of all samples decrease with increasing frequency. However, when the frequency exceeds 100 kHz, there is a tendency for the dielectric loss to increase. This is due to the presence of a resonance frequency between ion hopping and the external field, resulting in the transfer of electrical energy to oscillating ions. At the same time, with the increase of Co content, the $\tan\delta$ value decreases to 0.076 in $BiFe_{0.97}Co_{0.03}O_3$. In the low frequency region, it is mainly leakage current loss, while in the high frequency region, polarization relaxation dominates [59, 60]. The minimum $\tan\delta$ value of $BiFe_{0.97}Co_{0.03}O_3$ is related to the lowest leakage current and oxygen vacancy concentration. Overall, the results indicate that Co doping significantly alters the dielectric properties of BFO.

Using UV-visible absorption spectroscopy to study the optical properties of samples enables changes in the band
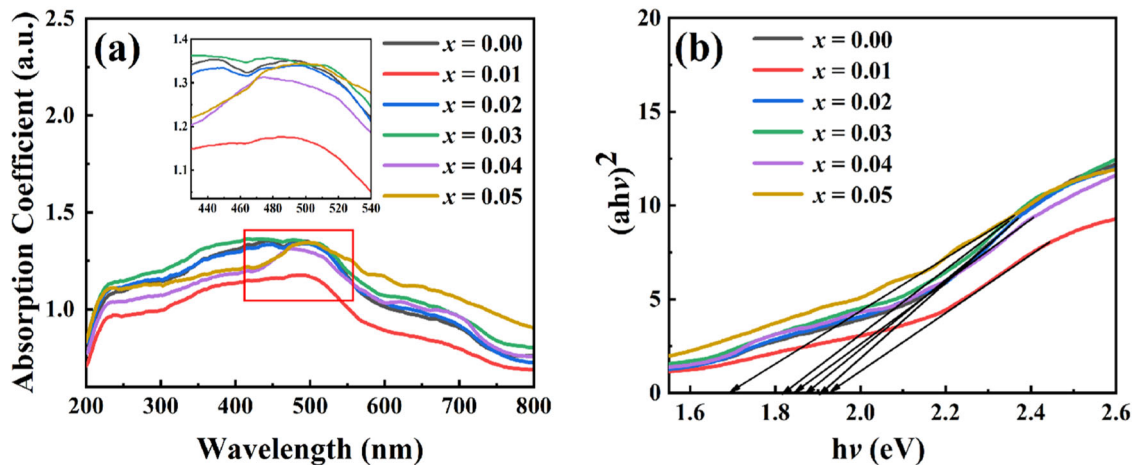
Fig. 9 **a** UV–Vis absorption spectra of the BFCO thin films. **b** Tauc curves of the BFCO thin films

structure and band gap of the samples to be explored, as shown in Fig. 9. The charge transfer of Bi-O occurs around 250–360 nm, while the charge transfer band of Fe-O corresponds to the peak around 490 nm. In Fig. 9a, all BFCO films show a noticeable absorption peak, with the maximum absorption wavelength around 500 nm, confirming the visible light response of all samples [61]. With the increase of Co doping concentration, the light absorption of the sample shows a red shift, and the width of the absorption peak increases. New energy levels appear when dopants are added, resulting in an increase in the density of states of the energy band, which corresponds to the generation of localized states in the energy band gap, thereby altering the density of states in the energy band. Estimation of the optical band gap for the corresponding sample is based on the Tauc equation and calculated using the formula $ahv = A(hv - E_g)^n$. Here, BFO is a direct band gap material, and the value of n is 1/2 [62]. Plotting the $(ahv)^2 - hv$ curve and extending its linear segment to intersect the x-axis will give the extrapolated optical band gap in Fig. 9b. The bandgap widths of $BiFe_{1-x}Co_xO$ (x = 0.00–0.05) are approximately 1.87 eV, 1.93 eV, 1.90 eV, 1.82 eV, 1.85 eV, and 1.69 eV, respectively. With the doping of Co, the band gap width shows a decreasing trend. This may be due to the lattice distortion of FeO_6 octahedra caused by Co doping, which in turn causes a slight strain in the sample structure and a reordering of molecular orbitals, thereby changing the range of visible light absorption. The research results can provide a reference for photodetectors and infrared detectors based on BFO thin films [63, 64].

4 Conclusion

This study systematically investigates the influence of Co ion substitution at the Fe site on $BiFeO_3$ (BFO) thin films

through the preparation of BFCO thin films (x = 0–0.05) on FTO/glass substrates using the sol–gel technique. XRD analysis confirms the perovskite rhombohedral structure of the BFMO thin films, with no secondary phases detected. SEM analysis combined with the XRD results indicates that Co doping leads to the formation of smaller and more uniformly distributed grains, resulting in reduced grain boundary resistance. This facilitates the reversal of ferroelectric domains and enhances polarization. The presence of Co is confirmed by EDS and XPS, which reveals a reduction in the concentrations of Fe^{2+} ions and oxygen vacancies. Consequently, this reduction contributes to the decrease in leakage current. Among the BFCO thin films, the $BiFe_{0.97}Co_{0.03}O_3$ thin film exhibits the highest remnant polarization ($P_r = 152.1\ \mu C/cm^2$) and the lowest leakage current density ($7.18 \times 10^{-7}\ A/cm^2$). The remnant polarization of the BFO thin film significantly increases with an increase in the applied electric field, while Ohmic conduction becomes the dominant leakage mechanism. Additionally, the bandgap of the BFO thin film decreases as the Co doping level increases, reaching a minimum value of 1.69 eV at x = 0.05. These findings demonstrate the effectiveness of Co doping in simultaneously reducing the bandgap and enhancing the ferroelectric behavior of BFO. Consequently, BFCO thin films hold promise as potential materials for the development of efficient ferroelectric photovoltaic devices.

Author contributions JZ wrote the main manuscript text and GCZ and XJZ prepared figures 1–3. All authors reviewed the manuscript.

Compliance with ethical standards

Conflict of interest The authors declare no competing interests.

References

1. Wang J, Neaton JB, Zheng H, Nagarajan V, Ogale SB, Liu B et al. (2003) Epitaxial $BiFeO_3$ multiferroic thin film heterostructures. Science 299:1719–1722

2. Van Aken BB, Rivera JP, Schmid H, Fiebig M (2007) Observation of ferrotoroidic domains. Nature 449:702–705

3. Hajra S, Oh Y, Sahu M, Lee K, Kim HG, Panigrahi BK, Mistewicz K, Kim HJ (2022) Piezoelectric nanogenerator based on flexible $PDMS-BiMgFeCeO_6$ composites for sound detection and biomechanical energy harvestingt. Energy Fuels 5:6049–6058

4. Kumar N, Shukla A, Kumar N, Sahoo S, Hajra S, Choudhary RNP (2018) Structural, electrical and ferroelectric characteristics of $Bi(Fe_{0.9}La_{0.1})O_3$. Ceram Int 44:21330–21337

5. Liu YQ, Wang Y, Ma J, Li S, Pan H, Nan CW, Lin YH (2022) Controllable electrical, magnetoelectric and optical properties of $BiFeO_3$ via domain engineering. Prog Mater Sci 127:100943

6. Eerenstein W, Mathur N, Scott JF (2006) Multiferroic and magnetoelectric materials. Nature 442:759–765

7. Fiebig M (2005) Revival of the magnetoelectric effect. J Phys D: Appl Phys 38:R123–R152

8. Wu JG, Fan Z, Xiao DQ, Zhu JG, Wang J (2016) Multiferroic bismuth ferrite-based materials for multifunctional applications: ceramic bulks, thin films and nanostructures. Prog Mater Sci 84:335–402

9. Spaldin NA, Cheong SW, Ramesh R (2010) Multiferroics: past, present, future. Phys Today 63:38

10. Ramesh R, Spaldin N (2007) Multiferroics: progress and prospects in thin films. Nat Mater 6:21–29

11. Catalan G, Scott JF (2009) Physics and applications of bismuth ferrite. Adv Mater 21(24):2463–2485

12. Yin LI, Mi W (2020) Progress in $BiFeO_3$-based heterostructures: materials, properties and applications. Nanoscale 12(2):477–523

13. Blázquez Martínez A, Godard N, Aruchamy N, Milesi-Brault C, Condurache O, Bencan A, Glinsek S, Granzow T (2021) Solution-processed $BiFeO_3$ thin films with low leakage current. J Eur Ceram Soc 41(13):6449–6455

14. Makhdoom AR, Akhtar MJ, Rafiq MA, Hassan MM (2012) Investigation of transport behavior in Ba doped $BiFeO_3$. Ceram Int 38:3829–3834

15. She S, Yu J, Tang W, Zhu Y, Chen Y, Sunarso J, Zhou W, Shao Z (2018) Systematic study of oxygen evolution activity and at ability on $La_{1-x}Sr_xFeO_{3-\delta}$ perovskite electrocatalysts in alkaline media. ACS Appl Mater Interfaces 10:11715–11721

16. Xue M, Tan G, Xia A, Chai Z, Lv L, Ren H, Ren X, Li J (2019) Multi-doped bismuth ferrite thin films with enhanced multiferroic properties. Ceram Int 45:12806–12813

17. Yu C, Viola G, Zhang D, Zhou K, Koval V, Mahajan A, Wilson RM, Tarakina NV, Abrahams I, Yan H (2018) Phase evolution and electrical behaviour of samarium-substituted bismuth ferrite ceramics. J Eur Ceram Soc 38:1374–1380

18. Biswas PP, Pal S, Subramanian V, Murugavel P (2019) Large photovoltaic response in rare-earth doped $BiFeO_3$ polycrystalline thin films near morphotropic phase boundary composition. Appl Phys Lett 114(17):173901

19. Bhatnagar A, Roy Chaudhuri A, Heon Kim Y, Hesse D, Alexe M (2013) Role of domain walls in the abnormal photovoltaic effect in $BiFeO_3$. Nat Commun 4(1):2835

20. Walker J, Bryant P, Kurusingal V, Sorrell C, Kuscer D, Drazic G, Bencan A, Nagarajan V, Rojac T (2015) Synthesis-phase-composition relationship and high electric-field-induced electromechanical behavior of samarium-modified $BiFeO_3$ ceramics. Acta Mater 83:149–159

21. Tan G, Chai Z, Zheng Y, Yue Z, Yang W, Guo M, Ren H, Xia A, Lv L, Liu Y (2018) Tunable structural transition and multiferroic properties of the composite thin films through the structural transition of magnetic layer. J Eur Ceram Soc 38:4463–4475

22. Kumar N, Shukla A, Choudhary RNP (2020) Effects of milling time on structural, electrical and ferroelectric features of mechanothermally synthesized multi-doped bismuth ferrite. Appl Phys 126:181

23. Yang SJ, Zhang FQ, Xie XB, Sun HJ, Zhang LP, Fan SH (2018) Enhanced leakage and ferroelectric properties of Zn-doped $BiFeO_3$ thin films grown by sol-gel method. J Alloy Compd 734:243–249

24. Sharma GN, Dutta S, Pandey A, Singh SK, Chatterjee R (2017) Microstructure and improved electrical properties of Ti-substituted $BiFeO_3$ thin films. Mater Res Bull 95:223–228

25. Priya AS, Geetha D (2021) Impact of (Zr, Cu) ion substitution on the optical, dielectric, and impedance behavior of $BiFeO_3$. Braz J Phys 51:40–46

26. Liu Y, Tan GQ, Guo MY, Chai ZJ, Lv L, Xue MT, Rena XX, Li JC, Ren HJ, Xia A (2019) Multiferroic properties of La/Er/Mn/Co multi-doped $BiFeO_3$ thin films,. Ceram Int 45:11765–11775

27. Qi X, Dho J, Tomov R, Blamire MG, MacManus-Driscoll JL (2005) Greatly reduced leakage current and conduction mechanism in aliovalent ion doped $BiFeO_3$. Appl Phys Lett 86(6):062903

28. Xue X, Tan G, Liu W, Hao H, Ren H (2015) Structural, electrical, and magnetic properties of multiferroic $Bi_{1-x}Gd_xFe_{0.97}Co_{0.03}O_3$ thin films. J Alloy Compd 622:477–482

29. Arya G, Yogiraj J, Negi NS, Shah J, Kotnala RK (2017) Observation of enhanced multiferroic, magnetoelectric and photocatalytic properties in Sm-Co codoped $BiFeO_3$ nanoparticles. J Alloy Compd 723:983–994

30. Sinha AK, Bhushan B, Jagannath, Gupta N, Sen S, Prajapat CL, Nuwad J, Bhatt P, Mishra SK, Meena SS, Priyam A (2020) Effect of cobalt-doping on dielectric, magnetic and optical properties of $BiFeO_3$ nanocrystals synthesized by sol-gel technique. Solid State Sci 102:106168

31. Saha S, Singh RP, Rout A, Mishra A, Ali A, Basumatary H, Ranjan R (2023) Inducing ferromagnetism and magnetoelectric coupling in the ferroelectric alloy system $BiFeO_3-PbTiO_3$ via additives. J Appl Phys 133:064101

32. Wani WA, Kundu S, Ramaswamy K, Venkataraman H (2020) Structural, morphological, optical and dielectric investigations in cobalt doped bismuth ferrite nanoceramics prepared using the sol-gel citrate precursor method. J Alloy Compd 846:156334

33. Eerenstein W, Mathur ND, Scott JF (2006) Multiferroic and magnetoelectric materials. Nature 442(7104):759–765

34. Deng XL, Zeng ZX, Gao RL (2020) Study of structural, optical and enhanced multiferroic properties of Ni doped BFO thin films synthesized by sol-gel method. J Alloy Compd 831:154857

35. Qi J, Liu H, Feng M, Xu H, Liu HW, Wang C, Wang AP, Lü WM (2020) Enhanced hydrogen evolution reaction in Sr doped $BiFeO_3$ by achieving the coexistence of ferroelectricity and ferromagnetism at room temperature. J Energy Chem 53:93–98

36. Li Z-J, Hou Z-L, Song W-L, Liu X-D, Cao W-Q, Shao X-H, Cao M-S (2016) Unusual continuous dual absorption peaks in Ca-doped $BiFeO_3$ nanostructures for broadened microwave absorption. Nanoscale 8:10415–10424

37. Singh MK, Jang HM, Ryu S, Jo MH (2006) Polarized Raman scattering of multiferroic $BiFeO_3$ epitaxial films with rhombohedral R3c symmetry. Appl Phys Lett 88:042907

38. Singh M, Jang H, Jo M, Ryu S (2006) Polarized Raman scattering of multiferroic $BiFeO_3$ epitaxial films with rhombohedral R3c symmetry. Appl Phys Lett 88:042907

39. Wang Y, Wang J (2009) Modulated charged defects and conduction behaviour in doped $BiFeO_3$. thin films, J Phys D: Appl Phys 42(16):162001

40. Bai L, Sun MJ, Ma WJ, Yang JH, Zhang JK, Liu YQ (2020) Enhanced magnetic properties of Co-doped $BiFeO_3$ thin films via structural progression. Nanomaterials 10:1798

41. Yue ZW, Tan GQ, Yang W, Ren HJ, Xiao A (2016) Enhanced multiferroic properties in Pr-doped $BiFe_{0.97}Mn_{0.03}O_3$ films. Ceram Int 42:18692–18699

42. Guo M, Tan G, Yang W, Liu Y, Ren H, Xia A, Lv L, Xue M (2018) Multiferroic properties of $Bi_{0.89}Ho_{0.08}Sr_{0.03}Fe_{0.97-x}Mn_{0.03}Ni_xO_3$ thin films modulated by F-N tunneling effects. Ceram Int 44:12282–12291

43. Ren XX, Tan GQ, Liu Y, Li JC, Xue MT, Ren HJ, Xia A, Liu WL, Liu Y (2020) Oxygen vacancy and grain boundary resistance regulate the intrinsic ferroelectric properties of $Bi_{0.96}Sr_{0.04}Fe_{0.98-x}Mn_xCo_{0.02}O_3$ thin film. J Eur Ceram Soc 44:5431–5440

44. Chai Z, Tan G, Yue Z, Xue M, Liu Y, Lv L, Ren H, Xia A (2018) Structural transition, defect complexes and improved ferroelectric behaviors of $Bi_{0.88}Sr_{0.03}Gd_{0.09}Fe_{0.94}Mn_{0.04}Co_{0.02}O_3/Co_{1-x}Mn_xFe_2O_4$ bilayer thin films. Ceram Int 44:15770–15777

45. Zhang Y, Qi J, Wang Y, Tian Y, Zhang J, Hu T, Wei M, Liu Y, Yang J (2018) Tuning magnetic properties of $BiFeO_3$ thin films by controlling Mn doping concentration. Ceram Int 44:6054–6061

46. Verma P, Singh P, Roy PK (2021) Influence on properties of $Bi_{0.9}Sm_{0.1}FeO_3$ multiferroic system with Mg substitution at Fe-site. J Solid State Chem 302:122432

47. Mocherla PSV, Karthik C, Ubic R, Ramachandra Rao MS, Sudakar C (2013) Tunable bandgap in $BiFeO_3$ nanoparticles: the role of microstrain and oxygen defects. Appl Phys Lett 103:022910

48. Kossar S, Amiruddin R, Rasool A, Giridharan NV, Dhayanithi D, Santhosh Kumar MC (2020) Ferroelectric polarization induced memristive behavior in bismuth ferrite ($BiFeO_3$) based memory devices. Superlattice Microst 148:106726

49. Jin LH, Tang XW, Wei RH, Yang BB, Yang J, Song WH, Dai JM, Zhu XB, Sun YP (2016) $BiFeO_3(001)/LaNiO_3/Si$ thin films with enhanced polarization: an all solution approach. RSC Adv 6:78629–78635

50. Liang XL, Dai JQ, Zhang GD (2022) Great ferroelectric properties and narrow bandgaps of $BiFeO_3$ thin films by (Mg, Mn) modifying. Appl Surf Sci 586:152751

51. Yu BF, Li MY, Hu ZQ, Pei L, Guo DY, Zhao XZ, Dong SX (2008) Enhanced multiferroic properties of the high-valence Pr doped $BiFeO_3$ thin film. Appl Phys Lett 93:182909

52. Dong G, Tan G, Luo Y, Liu W, Xia A, Ren H (2014) Charge defects and highly enhanced multiferroic properties in Mn and Cu co-doped $BiFeO_3$ thin films. Appl Surf Sci 305:55–61

53. Naganuma H, Inoue Y, Okamura S (2008) Evaluation of electrical properties of leaky $BiFeO_3$ films in high electric field region by high-speed positive-up-negativedown measurement. Appl Phys Express 1:061601

54. Wang J, Luo L, Han C, Yun R, Tang X, Zhu Y, Nie Z, Zhao W, Feng Z (2019) The microstructure, electric, optical and photovoltaic properties of $BiFeO_3$ thin films prepared by low-temperature sol-gel method. Materials 12:1444

55. Qi X, Dho J, Tomov R, Blamire MG, MacManus-Driscoll JL (2005) Greatly reduced leakage current and conduction mechanism in aliovalent-ion-doped $BiFeO_3$. Appl Phys Lett 86:062903

56. Wang C, Takahashi M, Fujino H, Zhao X, Kume E, Horiuchi T, Sakai S (2006) Leakage current of multiferroic $(Bi_{0.6}Tb_{0.3}La_{0.1})FeO_3$ thin films grown at various oxygen pressures by pulsed laser deposition and annealing effect. J Appl Phys 99:054104

57. Dai Y, Guo Q, Cui C, Yang L, Li C, Li X (2018) Role of ferroelectric/ferromagnetic layers on the ferroelectric properties of magnetoelectric composite films derived by chemical solution deposition. Mater Res Bull 99:424–428

58. Zhu J-H, Dai J-Q, Xu J-W, Li X-Y (2018) Effect of Zn and Ti Co-doping on structure and electrical properties of $BiFeO_3$ ceramics. Ceram Int 44:9215–9220

59. Chai ZJ, Tan GQ, Yue ZW, Xue MT, Liu Y, Lv L, Ren HJ, Xia A (2018) Structural transition, defect complexes and improved ferroelectric behavior of $Bi_{0.88}Sr_{0.03}Gd_{0.09}Fe_{0.94}Mn_{0.04}Co_{0.02}O_3/Co_{1-x}Mn_xFe_2O_4$ bilayer thin films. Ceram Int 44:15770–15777

60. Lin D-Y, Chen H-Z, Kao M-C, Zhang P-L (2020) Ferroelectric and electrical properties optimization of Mg-doped $BiFeO_3$ flexible multiferroic films. Symmetry 12(7):1173

61. Ramachandran B, Dixit A, Naik R, Lawes G, Rao MSR (2010) Charge transfer and electronic transitions in polycrystalline $BiFeO_3$. Phys Rev B 82:012102

62. Guo BL, Deng HM, Zhai XZ, Zhou WL, Meng XK, Weng GE, Chen SQ, Yang PX, Chu JH (2017) Cr doping-induced structural phase transition, optical tuning and magnetic enhancement in $BiFeO_3$ thin films. Mater Lett 186:198–201

63. Zhang S-T, Zhang Y, Lu M-H, Du C-L, Chen Y-F, Liu Z-G, Zhu Y-Y, Ming N-B, Pan XQ (2006) Substitution-induced phase transition and enhanced multiferroic properties of $Bi_{1-x}La_xFeO_3$ ceramics. Appl Phys Lett 88:162901

64. Chai Z, Tan G, Yue Z, Yang W, Guo M, Ren H, Xia A, Xue M, Liu Y, Lv L (2018) Ferroelectric properties of $BiFeO_3$ thin films by Sr/Gd/Mn/Co multi-doping. J Alloy Compd 746:677–687